Minimization of Flux and Torque Ripples of FPOEW Induction Motor with FCS-MPTC using Synthetic Voltage Vectors

Naresh Rayavarapu, Swati Devabhaktuni, *Member, IEEE*, and C. Venkata Subba Reddy

***Abstract*—This paper introduces a new topology for five-phase Open-end Winding Induction Motor (OEWIM) using Finite Control Set Model Predictive Torque Control (FCS-MPTC). This topology shows the enhancement in the steady-state performance by reducing flux and torque ripples and minimizing the percentage of total harmonic distortion (%THD) in stator current. The FCS-MPTC scheme proposed here employs a shared DC link for both inverters, ensuring zero common mode current, thereby eliminating the need for a large isolation transformer. This topology generates Synthetic Voltage Vectors (SVV) which result from the vector summation of the individual inverter Virtual Voltage Vectors(VVV). Common Mode Voltage (CMV) across the motor windings is nullified using this topology. Another notable aspect of FCS-MPTC is its ability to suppress high harmonic currents through the windings by reducing the average voltage in the non-torque-producing plane (x-y plane). Experimental validation compares the effectiveness of FCS-MPTC against traditional Three-Level Direct Torque Control (TL-DTC) and Five-Level Direct Torque Control (FL-DTC) methodologies.**

Link to graphical and video abstracts, and to code: https://latamt.ieeer9.org/index.php/transactions/article/view/9040

***Index Terms*—Three-Level Direct torque control (TL-DTC), Five-Level Direct torque control (FL-DTC), Finite-Control Set Model Predictive Torque Control (FCS-MPTC), Virtual Voltage Vectors(VVV), Synthetic Voltage Vector (SVV), Open-end Winding Induction Motor (OEWIM).**

I. INTRODUCTION

Extensive research has been conducted on multi-phase (Number of phases greater than three) induction motors (MPIM) because of their reliability, fault tolerance, and structurally redundant design [1]. Advantages of MPIM over traditional three-phase induction motors include decreased DC link current harmonics and rotor harmonic current losses, enhanced frequency with reduced amplitude of torque pulsations, minimized current per phase for a given power, improved power distribution per phase, precise control, and lower voltage requirements for high-power applications [2]. MPIM applications include submarines, aircraft, locomotive traction, Electric Hybrid Vehicles (EHV), rolling mills, and wind energy systems. The first odd phase configuration of MPIM next to the three-phase induction motor is a Five-Phase Induction Motor (FPIM), equipped with either distributed or concentrated types of stator winding, configured in star, pentagon, and pentacle. [3-4]. The 2-level inverter is sufficient to feed power to FPIM at low voltage and power ratings. When operating at high voltage and power ratings, utilizing conventional Multi-Level Inverters (MLI) is more advantageous. However, the traditional MLI configurations have significant drawbacks such as capacitor voltage unbalance in the case of Neutral Point Clamped (NPC), the requirement of multiple DC inputs in the case of Cascaded H-Bridge (CHB), and the need for additional capacitor banks in Flying Capacitor (FC). The open-end winding (OEW) scheme is free from all drawbacks mentioned above for MLI used for motor drive applications [5].

Advanced control techniques; Field Oriented Control (FOC) provides precise control over the speed and torque of the motor. This makes it particularly valuable for meeting the exacting requirements of industrial applications [6]. FOC relies on proportional-integral (PI) regulators, reference frame transformations, and rotor flux observers, all of which contribute to its intricate structure. Conversely, DTC is favored over FOC in certain applications because of its simplicity, rapid response, and robustness. DTC provides quicker torque response and exhibits lower sensitivity to parameter variations [7]. Model Predictive Control (MPC) offers superior dynamic response, decreased torque ripple, and enhanced efficiency by minimizing energy losses compared to DTC and FOC. MPTC's advantages over FOC and DTC are making it increasingly important for high-performance electric drives. [8]. The advantages include improved torque and flux regulation, simplified control facilitated by parameter regulation within a cost function, a straightforward structure, and intuitive operation [9]. The induction motor's dynamic torque control using MPTC will naturally support several control variables, nonlinear systems, and system constraints. [10]. The implementation of the mentioned advanced control schemes directly to multi-phase motors leads to phase current distortion and unnecessary power losses due to non-torque-producing components [11].For any 'n' multi-odd phase machines the generation of a pair of x-y plane harmonics is $\left(\frac{n-1}{2}\right)-1$.

To address the x-y plane harmonic component, extensive research has been conducted in the literature. The objectives of advanced control schemes in multi-phase motors include eliminating or minimizing the x-y plane harmonic components,

---

The associate editor coordinating the review of this manuscript and approving it for publication was Gabriel Pinto (*Corresponding author: Naresh Rayavarapu*).

N. Rayavarapu, S. Devabhaktuni, and C. V. S. Reddy are with National Institute of Technology, Warangal, India (e-mails: nr21eerer08@student.nitw.ac.in, swatikjm@nitw.ac.in, and cvsreddy@student.nitw.ac.in).

TABLE I
LITERATURE ON DTC-BASED OPEN-END WINDING CONFIGURATIONS OF FPIM

Reference	Control Technique	Inverter Level and No. of Switches	Torque and Flux Ripple	%THD	x-y Harmonics	Key Methodological Differences	Novelty and Contributions	Limitations of Work
[24]	3-level DTC	3 and 20	High	High	Eliminated	Use non-adjacent line voltage vectors and the average voltage will be zero in the x-y plane. Only 10VV within 10 sectors are used.	DC link voltage requirements were reduced by 47.37% which is suitable for EV applications and A lower switching frequency results in fewer losses.	Underutilization of the voltage vector of OEW configuration. leads to high torque and flux ripples and THD.
[25]	9-level DTC	3 and 20	Minimized	Minimized	Minimized	Modified lookup table with 10 sectors and 40 active vectors	Reduction of torque ripple, switching frequency, and flux instability issues at low speeds	High switching frequency due to utilizing four vectors in one control cycle leads to power loss. The need for Fast DSP controllers increases the difficulty of practical implementation. DC bus utilization decreases due to the selection of small vectors
[26]	5-level DTC	3 and 20	Minimized	Minimized	Eliminated	A Modified lookup table with 10 virtual adjacent and 10 virtual nonadjacent line voltage vectors	17 to 90% higher line voltage across the motor winding. Increased reliability and reduced switch voltage rating.	Still appreciable High torque and flux ripples. The selection of voltage vectors during operation might go out of the hysteresis band due to the band gap reduction.
[27]	5-level DTC	3 and 20	Minimized	12%	Eliminated	Modified lookup table Utilized 40VV within 20 sectors	Increased sector resolution, Fine control of flux and torque. More accurate vector selection.	High-speed DSP controllers are needed due to the increment in the number of sectors and vectors High switching frequency leads to higher loss. In volt-sec balance, the exact
[28]	7-level DTC	3 and 20	Minimized	-	Minimized	A modified lookup table utilized 30VV within 10 sectors	Minimized Torque, flux ripples, and THD	In volt-sec balance, the exact Need for fast operating switches and High-speed DSP controllers

CMV, flux/torque ripple, and achieving a constant switching frequency [12]. Initially, space vector pulse width modulation (SVPWM) techniques are implemented on FPIM, which encounter challenges such as inefficient DC link utilization and a lack of control during low-speed operation of the drive [13]. In [14], TL-DTC with a 2-level 5-leg inverter on FPIM is experimented with virtual vectors to eliminate x-y plane components. In [15], for an FPIM, a method is proposed to minimize torque ripple and maintain a constant switching frequency using a duty-based constant switching torque controller, without eliminating non-torque-producing harmonic plane components. In [16], Payami et al. attempted to improve the flux pattern under dynamics at low speed by using small vectors instead of zero vectors in a lookup table. In [17] DTC-based FPIM with CMV and current harmonics reduction is implemented, utilizing 22 vectors in the control scheme. In [18], Predictive Torque Control (PTC) for FPIM is introduced to achieve variable speed control and overcome DTC's complex structure. In [19], a progressive comparison of PTC algorithms for FPIM is implemented to overcome the drawbacks of variable switching frequency and higher torque ripple. In [20], a speed sensor-less PTC for FPIM using Space Vector Modulation (SVM) is implemented to overcome the challenge of multi-objective cost function and improve steady-state performance by eliminating the need for a noisy speed sensor. Literature on various MLI-fed three-phase drives has been published in [21-23].

Several academics have recently focused on investigating the Twin-inverter-controlled FPIM tabulated in TABLE I to explore the features associated with dual inverter architecture [24-28]. In [24], a Dual Inverter fed FPOEWIM with ten virtual voltage vectors is employed and a three-level hysteresis torque controller is utilized in DTC, the FPIM exhibits high flux and torque ripple and increased current harmonic content. In [25], a nine-level torque controller-based DTC is implemented to reduce flux and torque ripple. This method

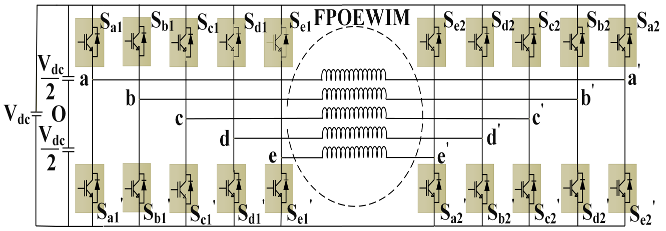

Fig. 1. Block diagram of the DI-fed FPOEW induction motor.

utilizes four sets of voltage vectors developed in a dual inverter-controlled FPOEWIM. However, the author overlooks the x-y plane components, leading to common-mode voltage and unnecessary power loss. A novel FL-DTC is introduced in [26] for an FPOEWIM with 20 virtual voltage vectors (VVV) to reduce flux ripple, torque ripple, and current THD. In [27], an FL-DTC scheme is implemented for FPOEWIM with 20 sectors and 40 virtual vectors to minimize torque and flux ripples compared with [26], and particularly targeted to achieve precise flux and torque control while eliminating CMV. The author of [28] built on work in [27] to minimize the torque and flux ripples and THD with 30 virtual voltage vectors to minimize the higher switching frequency.

The novelty of the proposed work in this paper mainly focuses on decreasing the higher flux and torque ripples, stator current THD, and x-y subspace harmonic currents of FPOWEIM with ten synthetic voltage vectors generated from identical dual inverter configurations. This work achieves the desired objectives without increasing the number of sectors and virtual voltage vectors. The cost function approach used in the proposed control method significantly eliminates x-y harmonic plane components compared with volt-sec balance method. The proposed method uses only large and medium voltage vectors which improve the dc bus utilization compared with multi-level hysteresis-based DTC schemes.

II. MODELLING OF FPOEW INDUCTION MOTOR WITH TWO-LEVEL VOLTAGE SOURCE INVERTER

Fig. 1 shows the block diagram of a three-level, two-identical voltage source inverter (VSI) that supplies power to an FPOEWIM with a common DC-link voltage ratio of 1:1. The pole voltages of Inverter-I and Inverter-II can be derived as follows:

$$\begin{pmatrix} V_{a0} \\ V_{b0} \\ V_{c0} \\ V_{d0} \\ V_{e0} \end{pmatrix} = \begin{pmatrix} S_{a1} \\ S_{b1} \\ S_{c1} \\ S_{d1} \\ S_{e1} \end{pmatrix} \cdot \frac{V_{dc}}{2} \tag{1}$$

$$\begin{pmatrix} V_{a'0} \\ V_{b'0} \\ V_{c'0} \\ V_{d'0} \\ V_{e'0} \end{pmatrix} = \begin{pmatrix} S_{a2} \\ S_{b2} \\ S_{c2} \\ S_{d2} \\ S_{e2} \end{pmatrix} \cdot \frac{V_{dc}}{2} \tag{2}$$

where $S_{a1}^{'}$, $S_{b1}^{'}$,$S_{c1}^{'}$, $S_{d1}^{'}$, $S_{e1}^{'}$ and $S_{a2}^{'}$, $S_{b2}^{'}$,$S_{c2}^{'}$, $S_{d2}^{'}$, $S_{e2}^{'}$ are the lower switching side of Inverter-I and Inverter-II phase legs respectively. The resultant phase leg voltage is shown in equation (3) and it has three levels in the dual identical inverter configurations.

$$\begin{pmatrix} \Delta V_{aa'} \\ \Delta V_{bb'} \\ \Delta V_{cc'} \\ \Delta V_{dd'} \\ \Delta V_{ee'} \end{pmatrix} = \begin{pmatrix} V_{a0}-V_{a'0} \\ V_{b0}-V_{b'0} \\ V_{c0}-V_{c'0} \\ V_{d0}-V_{d'0} \\ V_{e0}-V_{e'0} \end{pmatrix} \tag{3}$$

$$V_{cm}=\frac{1}{5}\cdot\left(\Delta V_{aa'}+\Delta V_{bb'}+\Delta V_{cc'}+\Delta V_{dd'}+\Delta V_{ee'}\right) \tag{4}$$

$$\begin{pmatrix} V_{aa'} \\ V_{bb'} \\ V_{cc'} \\ V_{dd'} \\ V_{ee'} \end{pmatrix} = \begin{pmatrix} \Delta V_{aa'} \\ \Delta V_{bb'} \\ \Delta V_{cc'} \\ \Delta V_{dd'} \\ \Delta V_{ee'} \end{pmatrix} - (V_{cm}) \tag{5}$$

The common mode voltage (CMV) and phase voltage are shown in equation (4) and (5) are obtained by solving equations (1), (2), and (3) of dual inverter configuration. A rigid coupling between the voltage and torque equations of induction motors, and their time-varying nature, enhances the difficulty of analyzing the dynamic behavior of the Induction motor. In modelling the conversion of five-phase quantities into two-phase quantities makes things straightforward and easier to analyze. Modelling of a five-phase induction motor using the following equations in a stationary reference frame, one can visualize the dynamic behavior of an induction motor. Space vector form of stator voltage:

$$V_s=R_s i_s+\frac{d}{dt}\psi_s \tag{6}$$

Space vector form of rotor voltage equation:

$$0=R_r i_r+\frac{d}{dt}\psi_r-\omega_r\psi_r \tag{7}$$

Space vector from of stator voltage in x-y reference:

$$v_{xys}=R_s i_{xys}+L_{ls}\frac{di_{xys}}{dt} \tag{8}$$

Arriving the stator flux linkages using equations (6) and (7) are:

$$\psi_s=\int\left(V_s-i_s R_s\right)\,dt \tag{9}$$

The stator and rotor flux linkages are as follows:

$$\psi_s=L_s i_s+L_m i_r \tag{10}$$

$$\psi_r=L_r i_r+L_m i_s \tag{11}$$

where $V_s, R_s, i_s, \psi_s, \psi_r, i_r, L_{ls}, v_{xys}, i_{xys}, andL_m$ are Stator Voltage vector, Stator Resistance, Stator current vector, Stator flux vector, Rotor Flux vector, Rotor current vector, Stator Leakage inductance, stator voltage vector of third harmonic plane, stator current of third harmonic plane and mutual inductance respectively.

The electromagnetic torque of the two-axis machine model is:

$$T_e=\frac{5}{2}\frac{P}{2}imag\left(\psi_s\cdot i_s\right) \tag{12}$$

Rotor speed from the torque balance equation is observed as:

$$\omega_r=\int\frac{T_e-T_l}{J}\,dt \tag{13}$$

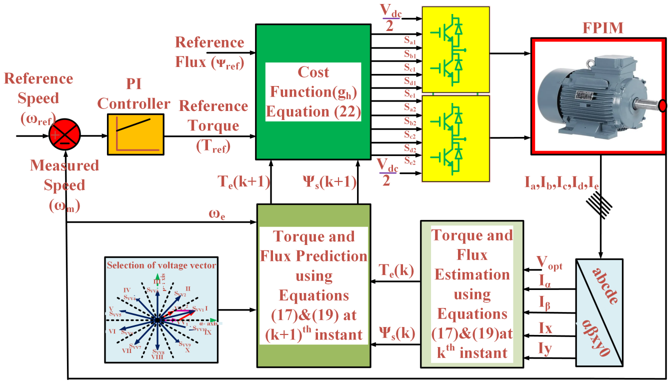

Fig. 2. Block diagram of FCS-MPTC-based Dual inverter fed FPOEWIM.

P is the Poles of Stator, T$_e$ is Electromagnetic torque, T_l is load torque, ω_r the mechanical speed of the rotor and J is the Moment of inertia.

III. PROPOSED FINITE CONTROL SET MODEL PREDICTIVE TORQUE CONTROL FOR FPOEWIM

Fig. 2. Depicts an FPOEWIM fed from a 3-level dual VSI. Using the equations from (6) to (13) of dynamic modeling of induction motors in the stationary reference frame, the stator current and rotor flux are derived as state variables shown in equations (14) and (15):

$$i_s + \ \tau_s \frac{di_s}{dt} = \frac{k_r}{R_\sigma}\left(\frac{1}{\tau_r} - j\omega\right)\psi_r + v_s R_\sigma \tag{14}$$

$$\psi_r + \ \tau_r \frac{di_s}{dt} = \ (j\omega)\,\tau_r \psi_r + L_m i_s \tag{15}$$

where

$$i_s = \ i_{ds} + j i_{qs}, \quad \psi_r = \psi_{dr} + j\psi_{qr}\ , \ v_s = v_{ds} + j v_{qs},$$

$$\tau_r = L_r R_r, \ \tau_\sigma = \sigma L_s R_\sigma, \ \ \sigma = 1 - \frac{L_m^2}{L_s L_r}\ , \qquad k_r = \ \frac{L_m}{L_r}\ ,$$

$$R_\sigma = R_s + R_r\ k_r^2\ , \quad and \quad \omega = P\omega_r;$$

The five-phase stator currents and motor speed are sensed from the machine during the operation of drive for the estimation of stator flux, torque, and speed error. The transformation matrices shown in equation (16) with $\theta = 2\pi/5$, are used to obtain two-phase currents from the sensed five-phase currents:

$$\begin{pmatrix} I_d \\ I_q \\ I_x \\ I_y \\ I_0 \end{pmatrix} = \frac{2}{5} \cdot \begin{pmatrix} 1 & cos\theta & cos2\theta & cos3\theta & cos4\theta \\ 0 & sin\theta & sin2\theta & sin3\theta & sin4\theta \\ 1 & cos3\theta & cos6\theta & cos9\theta & cos12\theta \\ 0 & sin3\theta & sin6\theta & sin9\theta & sin12\theta \\ 1/2 & 1/2 & 1/2 & 1/2 & 1/2 \end{pmatrix} \begin{pmatrix} I_a \\ I_b \\ I_c \\ I_d \\ I_e \end{pmatrix} \tag{16}$$

The error in speed is obtained by comparing the sensed actual speed ω_m with the reference speed ω_{ref} and it undergoes processing via the speed PI controller, ultimately yielding the reference torque command (T_{ref}). During experimentation, the amplitude of the reference torque would be within the nominal torque (T_{nom}). By applying forward Euler discretization at the instant (k+1) to the equations (6) and (14) the prediction equations (17) and (18) for stator flux and stator current are derived:

$$\psi_s^p\,(k+1) = \ \psi_s\,(k) + T_s v_s\,(k) - R_s T_s i_s\,(k) \tag{17}$$

$$\psi_s^p\,(k+1) = \left(1 + \frac{T_s}{\tau_\sigma}\right) i_s\,(k) + \frac{T_s}{\tau_\sigma + T_s} \cdot$$

$$\left\{\frac{1}{R_\sigma}\ \left[\left(\frac{k_r}{\tau_r} - j\omega k_r\right)\psi_r\,(k) + v_s\,(k)\right]\right\} \tag{18}$$

$$\psi_s = \psi_{ds} + j\psi_{qs}; \quad \psi_s^p\,(k+1) = \ \psi_{ds}^p\,(k+1) + j\psi_{qs}^p\,(k+1)$$

where T_s is sampling time and $v_s\,(k)$ is the resultant optimal voltage vector, here $v_s\,(k) = v_{s1}\,(k) - v_{s2}\,(k)$. $v_{s1}\,(k)$ is the virtual voltage vector generated with large and medium voltage vectors of the fundamental plane of Inverter-I at kth instant. Similarly $v_{s2}\,(k)$ is virtual voltage vector generated for Inverter-II at kth instant. The predicted electromagnetic torque from the predicted stator flux and stator current is expressed as:

$$T_e^p\,(k+1) = \frac{5}{2}\ P I_m\{(\ \psi_s^p\,(k+1) \cdot \ i_s^p\,(k+1)\} \tag{19}$$

The predicted x-y sub-space harmonic currents are derived using equation (8) as follows:

$$i_{xs}^p\,(k+1) = i_{xs}\,(k) + \frac{1}{L_{ls}}\,(T_s v_{xs}\,(k) - R_s T_s i_{xs}\,(k)) \tag{20}$$

$$i_{ys}^p\,(k+1) = i_{ys}\,(k) + \frac{1}{L_{ls}}\,(T_s v_{ys}\,(k) - R_s T_s i_{ys}\,(k)) \tag{21}$$

In the cost function shown in equation (22) the predicted values of torque and flux are compared with the reference values $T_{ref}\ and\ \psi_{ref}$. $i_{xs\ ref}$ and $i_{ys\ ref}$ is set to zero for the elimination of x-y harmonic currents.

$$g_h = \left|T_{ref} - T_e^p\,(k+1)_h\right| + \lambda_\psi \left|\psi_{ref} - \psi_s^p\,(k+1)_h\right|$$

$$+K_1 \cdot |0 - i_{xs}^2\ | + K_2 \cdot |\,0 - i_{ys}^2| \tag{22}$$

Cost function with the lowest error initiates the selection of an optimal voltage vector for the operation of inverter throughout the control cycle. The weighting factors $\lambda_\psi,\ K_1,\ and\ K_2$ are the control relative weights of flux and harmonic currents. The values of the weighting factors are obtained by referring [29] and observed as $\lambda_\psi = 0.85$, K_1= 0.255, K_2= 0.255. T_{nom} and $|\psi_{nom}|$ are the nominal values of torque and flux respectively. Horizon $h \ \in$ [0, 1, ……..12] and superscript p denotes prediction of quantities.

A. Space Voltage Vectors of Individual Inverters

In α-β and x-y subspace of a two-level five-leg VSI has 30 active switching vectors (shown in Fig. 3) and 02 are zero voltage vectors. Thirty active voltage vectors are split into 10 large, 10 medium, and 10 small vectors. In the α-β plane, the large voltage vectors (highlighted in blue) are mapping to the small voltage vectors in the x-y subspace and small voltage vectors in the α-β plane (highlighted in green) are mapped to x-y subspace with distinct phase angles. The α-β fundamental plane exhibits a comparable mapping to the medium voltage vectors (shown in red) in the x-y subspace. The equation (25)

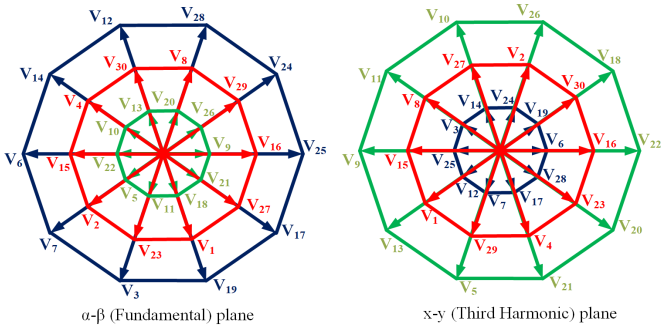

α-β (Fundamental) plane

x-y (Third Harmonic) plane

Fig. 3. Space voltage vectors for a five-phase inverter.

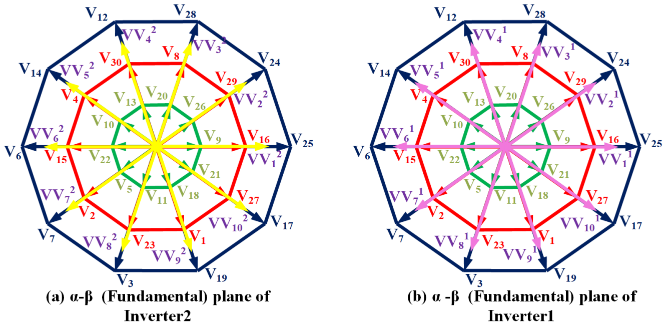

(a) α-β (Fundamental) plane of Inverter2

(b) α -β (Fundamental) plane of Inverter1

Fig. 4. Space VVV of (a) Inverter-II and (b) Inverter-I.

demonstrates how the resultant voltage space vector V_s of the dual inverter system is represented using the space voltage vectors V_{s1} and V_{s2} shown in equation (23) and (24) of individual VSI in the α-β plane. Zero voltage vectors are formed when all lower or upper switches of any inverters are turned on simultaneously, or when Inverter-I and Inverter-II are in a similar switching state:

$$V_{s1}=\frac{2}{5}\left(\frac{V_{dc}}{2}\right)\left(S_{a1}+S_{b1}e^{-\frac{i2\pi}{5}}+S_{c1}e^{-\frac{i4\pi}{5}}+\right.$$
$$\left.S_{d1}e^{-\frac{i6\pi}{5}}+S_{e1}e^{-\frac{i8\pi}{5}}\right) \tag{23}$$

$$V_{s2}=\frac{2}{5}\left(\frac{V_{dc}}{2}\right)\left(S_{a2}+S_{b2}e^{-\frac{i2\pi}{5}}+S_{c2}e^{-\frac{i4\pi}{5}}+\right.$$
$$\left.S_{d2}e^{-\frac{i6\pi}{5}}+S_{e2}e^{-\frac{i8\pi}{5}}\right) \tag{24}$$

$$V_s = V_{s1} - V_{s2} \tag{25}$$

In the α-β plane, large voltage vectors (highlighted in green) look like small voltage vectors in the harmonic subspace, or vice versa. With distinct phase angles, the α-β fundamental space exhibits a comparable mapping of the medium voltage vectors (shown in red) in the harmonic subspace. The switching states for a 2-level five-leg inverter are: $V_1(00001)$, $V_2(00010)$, $V_3(00011)$, $V_4(00100)$, $V_5(00101)$, $V_6(00110)$, $V_7(00111)$, $V_8(01000)$, $V_9(01001)$, $V_{10}(01010)$, $V_{11}(01011)$, $V_{12}(01100)$, $V_{13}(01101)$, $V_{14}(01110)$, $V_{15}(01111)$, $V_{16}(10000)$, $V_{17}(10001)$, $V_{18}(10010)$, $V_{19}(10011)$, $V_{20}(10100)$, $V_{21}(10101)$, $V_{22}(10110)$, $V_{23}(10111)$, $V_{24}(11000)$, $V_{25}(11001)$, $V_{26}(11010)$, $V_{27}(11011)$, $V_{28}(11100)$, $V_{29}(11101)$, $V_{30}(11110)$, $V_{31}(11111)$, $V_{32}(00000)$. The magnitude and angle of each space voltage vector can be derived from the corresponding switching states.

B. Generation of Synthetic Voltage Vectors (SVV)

In the proposed dual inverter configuration, the α-β space vector planes are divided into ten sectors represented in Fig. 4 each with a 36° angle span. The virtual voltage vectors VV_1^1 to VV_{10}^1 shown in Fig. 4(b) of the Inverter-I are generated by utilizing the active large space voltage vectors (V_{25} to V_{17}) and medium active space voltage vectors (V_{16} to V_{27}) of fundamental plane shown in Fig. 3.

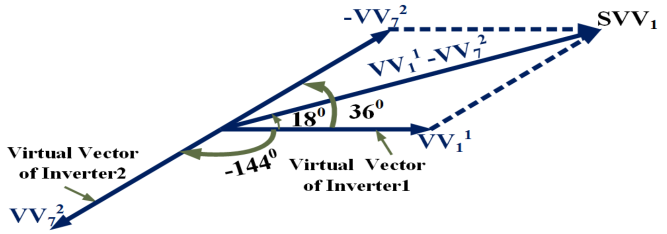

Fig. 5. Resultant synthetic voltage vector of the dual inverter.

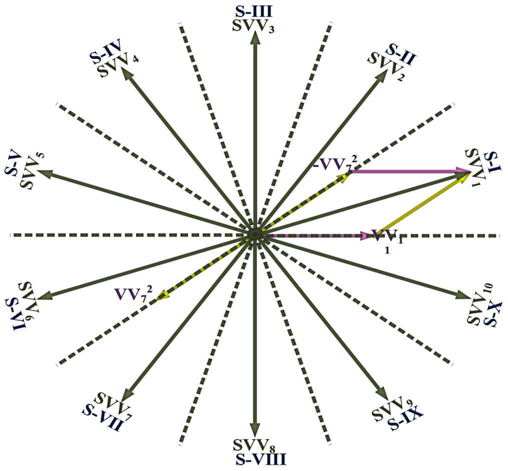

Fig. 6. Resultant synthetic voltage vectors of the dual inverter.

Similarly, the virtual voltage vectors VV_1^2 to VV_{10}^2 shown in Fig. 4(a) of Inverter-II are generated by utilizing the large (V_{25} to V_{17}) and medium (V_{16} to V_{27}) voltage vectors of fundamental (α-β) space shown in Fig. 3. VV_1^1 is the vector sum of two in line active space voltage vectors V_{25} and V_{16} and VV_{10}^1 is vector sum of V_{17} and $V_{27.}$ Similarly for the Inverter-II virtual voltage vectors $VV_1^2$and VV_{10}^2 are generated. The synthetic voltage vector $SVV_1 = VV_1^1 - VV_7^2$ for dual inverter is generated from the vector sum of virtual voltage vectors of Inverter-I (VV_1^1) and Inverter-II (VV_7^2) is shown in Fig. 5. The phase shift between virtual voltage vector of inverters is considered as 144 degrees to eliminate the common mode voltage (CMV). Similarly, the generation of remaining SVV_2 to SVV_{10} shown in Fig.6 and tabulated with their magnitude and corresponding angles in Table II.

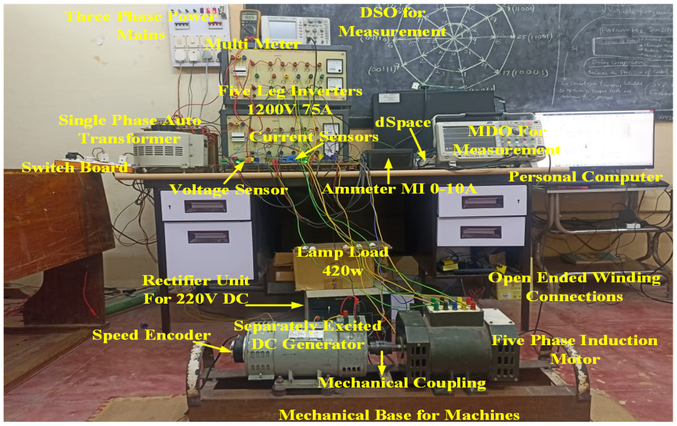

Fig. 7. Experimental Setup: Five-phase Open-ended Winding Induction Motor

TABLE II
RESULTANT SVV OF DUAL INVERTER

INVERTER -I (VVV)	INVERTER -II (VVV)	Resultant SVV
$VV_1^1 = V_{25}, V_{16}$	$VV_7^2 = V_7, V_2$	$SVV_1 = VV_1^1 - VV_7^2$
$VV_2^1 = V_{24}, V_{29}$	$VV_8^2 = V_3, V_{23}$	$SVV_2 = VV_1^1 - VV_8^2$
$VV_3^1 = V_{28}, V_8$	$VV_9^2 = V_{19}, V_1$	$SVV_3 = VV_3^1 - VV_9^2$
$VV_4^1 = V_{12}, V_{30}$	$VV_{10}^2 = V_{17}, V_{27}$	$SVV_4 = VV_4^1 - VV_{10}^2$
$VV_5^1 = V_{14}, V_4$	$VV_1^2 = V_{25}, V_{16}$	$SVV_5 = VV_5^1 - VV_1^2$
$VV_6^1 = V_6, V_{15}$	$VV_2^2 = V_{24}, V_{29}$	$SVV_6 = VV_6^1 - VV_2^2$
$VV_7^1 = V_7, V_2$	$VV_3^2 = V_{28}, V_8$	$SVV_7 = VV_7^1 - VV_3^2$
$VV_8^1 = V_3, V_{23}$	$VV_4^2 = V_{12}, V_{30}$	$SVV_8 = VV_8^1 - VV_4^2$
$VV_9^1 = V_{19}, V_1$	$VV_5^2 = V_{14}, V_4$	$SVV_9 = VV_9^1 - VV_5^2$
$VV_{10}^1 = V_{17}, V_{27}$	$VV_6^2 = V_6, V_{15}$	$SVV_{10} = VV_{10}^1 - VV_6^2$

C. Dwell Time Calculations of Virtual Vectors

The resultant synthetic voltage vectors of the inverter are applied to FPOEWIM between an interval 0 to T_s in every control cycle for its operation. The active space voltage vectors in the α-β plane are divided as large, medium, and small voltage vectors have magnitudes are 0.6472V$_{dc}$, 0.4V$_{dc}$, and 0.2472V$_{dc}$ respectively, mapping with α-β plane in x-y subspace voltage vectors has the magnitude of 0.2472V$_{dc}$, 0.4V$_{dc}$, and 0.6472V$_{dc}$. In order to eliminate x-y harmonic plane components with the FCS-MPTC the small subspace voltage vector V$_{25}$ in x-y plane must operate more time than the medium subspace voltage vector V$_{16}$ in one control (0 to T_s). Dwell times T_1 *and* T_2 are calculated by solving the equations (26) and (27) developed by equating the volt-second balance to zero in the x-y plane.

$$V_{25} \cdot T_1 - V_{16} \cdot T_2 = 0 \tag{26}$$

$$0.2472 \cdot V_{dc} \cdot T_1 - -0.4 \cdot V_{dc} \cdot T_2 = 0 \text{ (In x-y subspace)}$$

$$T_1 + T_2 = T_s \tag{27}$$

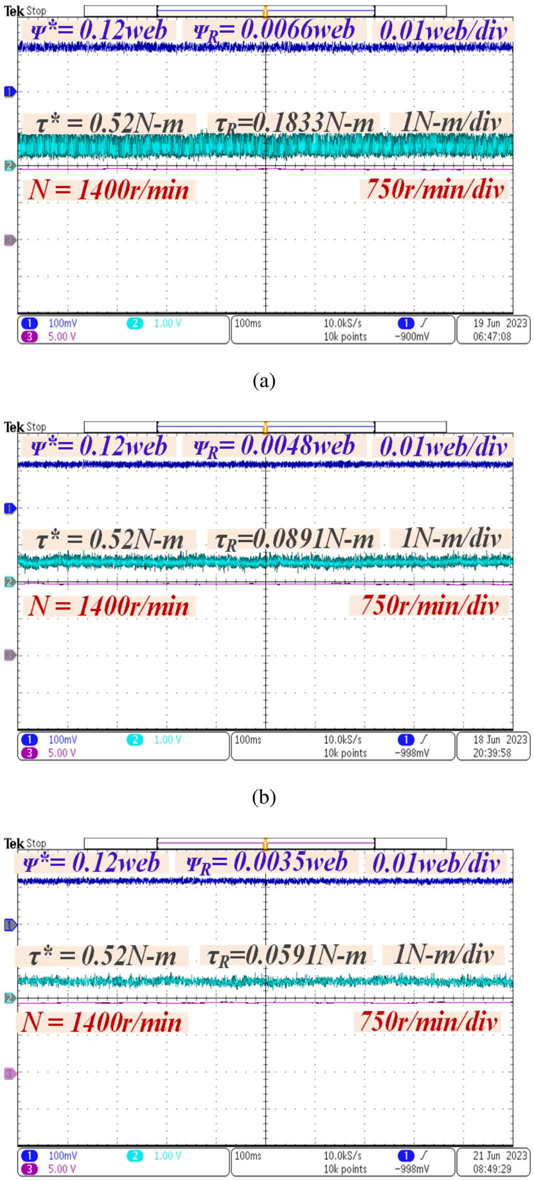

(a)

(b)

(c)

Fig. 8. Flux, Torque, and Speed under No-Load at 1400 r/min (a) TL-DTC (Left) (b) FL-DTC (Middle) (c) FCS-MPTC (Right).

$$T_1 = 0.618 \cdot T_s; T_2 = 0.382 \cdot T_s$$

For dual inverter configuration, the synthetic voltage vector magnitude and angle in the α-β plane concerning dwell times are as follows:

$$SVV_1 = VV_1^1 - VV_7^2$$

$$SVV_1 = \frac{V_{25}T_1 + V_{16}T_2}{T_s} - \frac{V_7T_1 + V_2T_2}{T_s}$$

$$SVV_1 = \frac{0.6472\angle 0 \cdot 0.618T_s + 0.4\angle 0 \cdot 0.382T_s}{T_s} -$$

$$\frac{0.6472\angle -144 \cdot 0.618T_s + 0.4\angle -144 \cdot 0.382T_s}{T_s} = 1.05\angle 18.$$

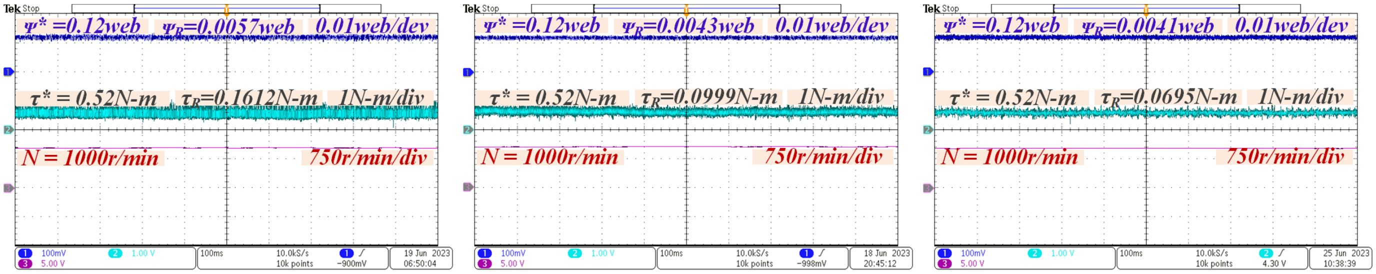

(a) (b) (c)

Fig. 9. Flux, Torque, and Speed under No-Load at 1000 r/min (a) TL-DTC (Left) (b) FL-DTC (Middle) (c) FCS-MPTC (Right).

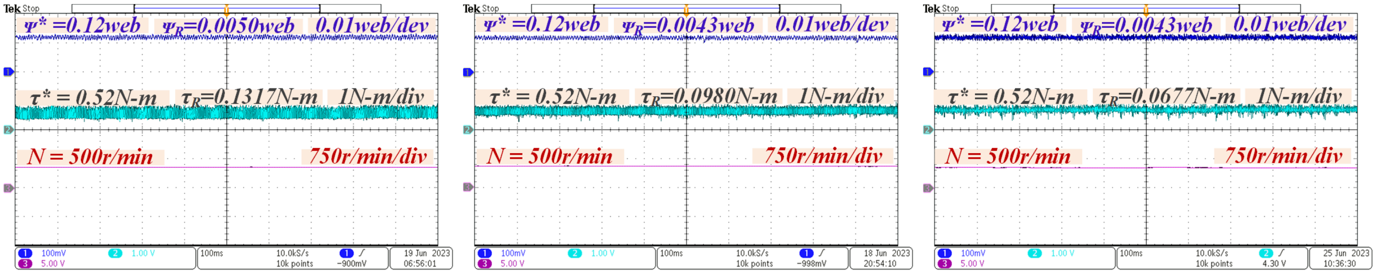

(a) (b) (c)

Fig. 10. Flux, Torque, and Speed under No-Load at 500 r/min (a) TL-DTC (Left) (b) FL-DTC (Middle) (c) FCS-MPTC (Right).

IV. EXPERIMENTAL RESULTS

The proposed FCS-MPTC scheme is experimented on an FPOWEIM drive. It comprises a 1.12 kW, 200 V, 3.4 A five-phase induction motor with an open-end stator winding configuration. The motor is mechanically coupled to a 0.75 kW, 220V, 3.4A separately excited DC generator for steady state and dynamic loading. 1024 Pulse Per Revolution (PPR) speed encoder and enhanced quadrature pulse (eQEP) peripheral in dSpace (MicrolabBox-1202) are interfaced to measure mechanical speed ω_m. Four LEM-make LA25-PCS hall effect sensors are interfaced to measure phase currents and the LV25-PVS hall effect sensor is interfaced for DC link voltage measurement. A single-phase autotransformer rated 0-240-270 volts 15 A feeds power to the rectifier unit in Semikron (SKM21F) 1200 V/75 A IGBT-based five-leg identical voltage source inverter power modules. The inverter power modules have an inbuilt driver circuit board with an appropriate dead band to feed the power to the motor. The machine was driven by standard Semikron (SKM21F) five-phase voltage source inverters the DC link voltage was set to 110 V because the DC link voltages required in OEW configurations are less, which feeds the motor drive from both ends. A dSpace (MicrolabBox) 1202/1302 controller with host Personal Computer (PC) for implementing control algorithm. TEKTRONICS 3024 Mixed Domain Oscilloscope (MDO) is used for capturing all the results. A lamp load of 230 V and 420 Watts is used for loading.

TABLE IV represents the five-phase induction motor parameters for the experimentation of all the control techniques, which are obtained with the help of stand-still tests. The power-fed FPIM is experimented with the proposed FCS-MPTC method and compared with TL-DTC and FL-DTC. Fig. 6 provides a picture of the entire system as a schematic rig. All three control techniques are experimented with at a sampling time of 100 μs which could be allowed for motor drives.TL-DTC, FL-DTC, and proposed FCS-MPTC methods are implemented at the nominal (rated) flux of 0.2 Wb and the nominal (rated) torque of 5 N-m. The experimented results shown from Fig. 8 to Fig. 22, of TL-DTC [24], FL-DTC [26], and the proposed FCS-MPTC methods are discussed in the following sections.

A. Analysis of Steady-State Performance

The performance motors under the steady state of existing and proposed methods are experimented with and analyzed at high, medium, and low speeds. Speeds considered for analysis are, 1000 r/min, 500 r/min, and 200 r/min, under No-Load/Lightly Loaded to full load conditions of induction motor. A data of 10000 samples (N)/s are considered to compute mean torque and flux ripples for all the methods using the following equation.

$$Torque/Flux_{ripple} = \sqrt{\frac{1}{N}\sum_{i=1}^{N}(Z_i - Z_{avg})^2} \tag{28}$$

Where Z_i is the flux/torque value at the i^{th} instant

Z_{avg} is the average flux/torque over N samples.

1) No-load and Loaded Analysis: In Fig. (8) – (11) A light load of 0.52 N-m is observed on the motor during no-load conditions for the speeds 1400 r/min, 1000 r/min, 500

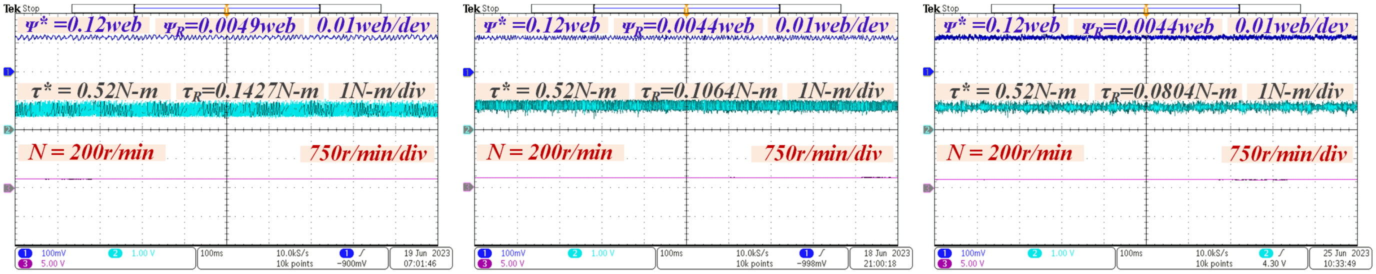

(a) (b) (c)

Fig. 11. Flux, Torque, and Speed under No-Load at 200 r/min (a) TL-DTC (Left) (b) FL-DTC (Middle) (c) FCS-MPTC (Right).

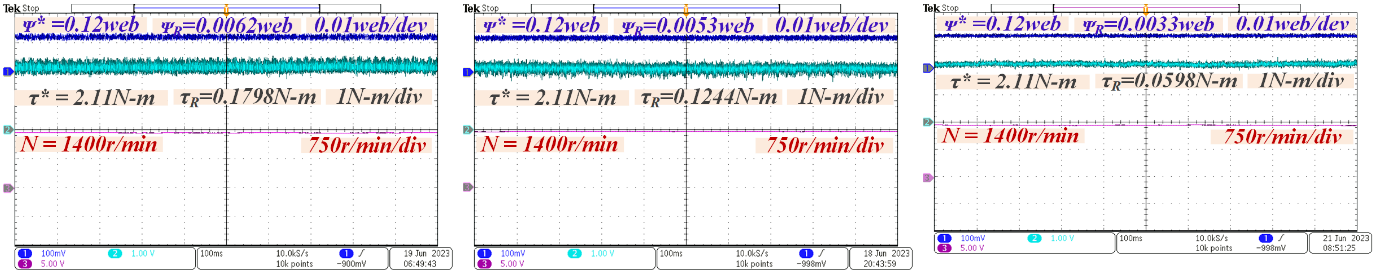

(a) (b) (c)

Fig. 12. Flux, Torque, and Speed at 2.11 N-m, and 1400 r/min, a) TL-DTC (Left) b) FL-DTC (Middle) c) FCS-MPTC (Right)

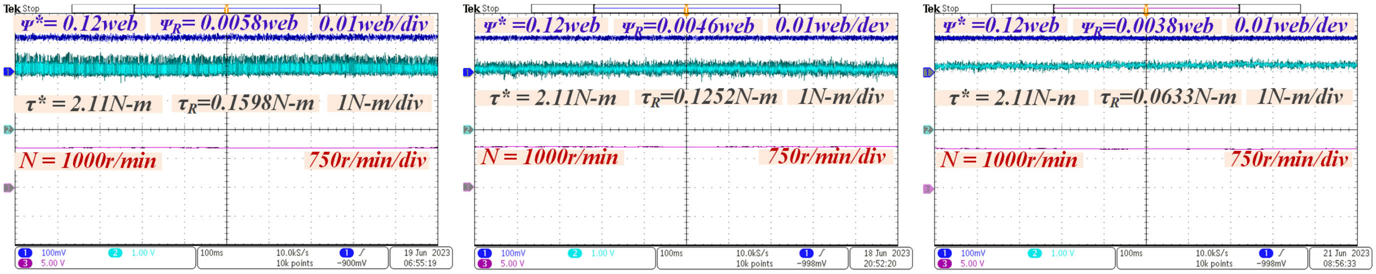

(a) (b) (c)

Fig. 13. Flux, Torque, and Speed at 2.11 N-m, and 1000 r/min, a) TL-DTC (Left) b) FL-DTC (Middle) c) FCS-MPTC (Right)

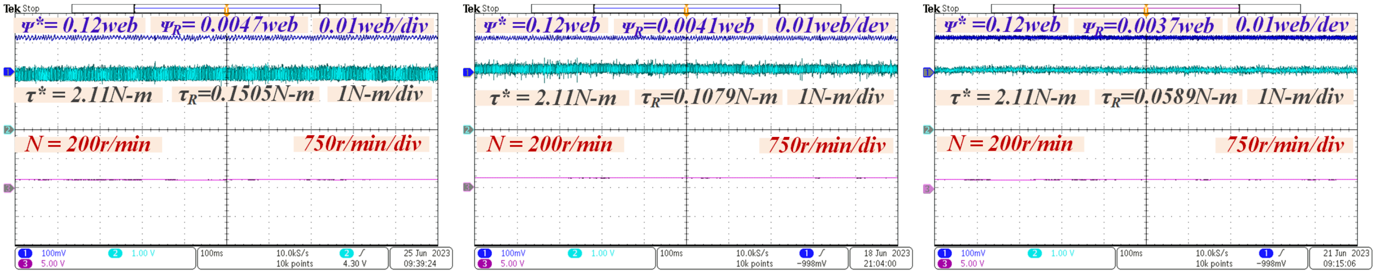

(a) (b) (c)

Fig. 14. Flux, Torque, and Speed at 2.11 N-m, and 500 r/min, a) TL-DTC (Left) b) FL-DTC (Middle) c) FCS-MPTC (Right)

r/min, and 200 r/min. Fig. 8(c) shows the steady state stator flux, Torque, and speed at 1400 r/min of the proposed control technique, it can be noticed that the stator flux and torque ripples are 0.0035 Wb and 0.059 N-m respectively. The steady-state stator flux and Torque ripples for the existing methods that is TL-DTC in Fig. 8(a) and FL-DTC in Fig. 8(b) are observed as 0.0066 Wb and 0.1833 N-m and 0.0048 Wb, 0.0891 N-m respectively. The torque ripple is reduced

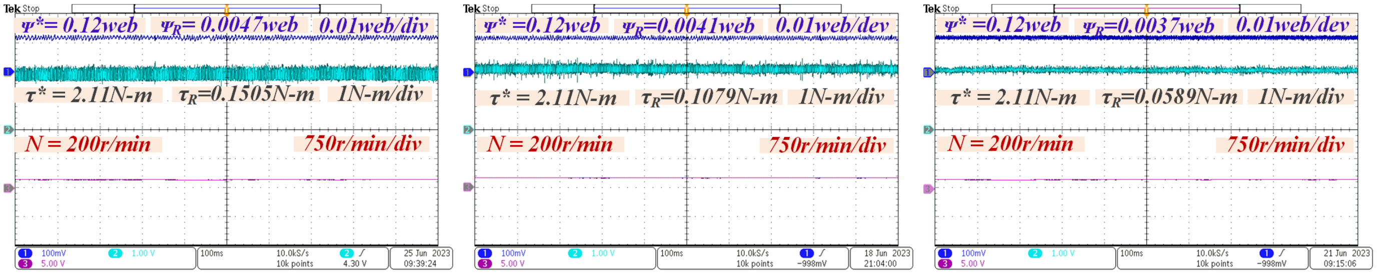

(a) (b) (c)

Fig. 15. Flux, Torque, and Speed at 2.11 N-m, and 200 r/min, a) TL-DTC (Left) b) FL-DTC (Middle) c) FCS-MPTC (Right)

TABLE III
PARAMETERS AND RATINGS OF FPIM

Symbol	Quantity	Units
R_s	Resistance of stator	1.05 ohms
R_r	Resistance of rotor	1.42 ohms
L_s	Stator Self Inductance	90 mH
L_r	Rotor Self Inductance	90 mH
L_{ls}	Stator Leakage Inductance	6 mH
L_{lr}	Rotor Leakage Inductance	6 mH
L_m	Magnetizing Inductance	84.73 mH
P	Number of Poles	4
J	Moment of Inertia	0.00148
T_s	Sampling Time	100 micro-Sec
V_{dc}	DC Link Voltage	200 Volts
I_L	LLine Current	3.4 Amps
P_m	Power Rating	1.12 kW

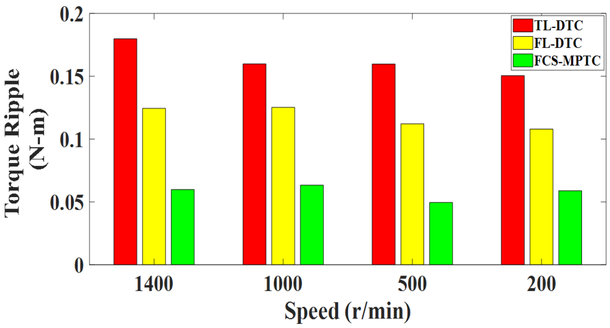

Fig. 16. Torque ripple at a load of 2.11 N-m.

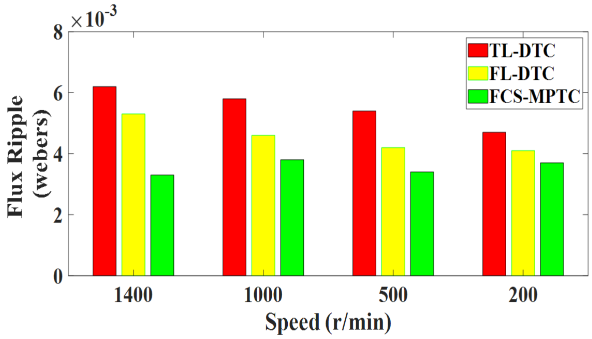

Fig. 17. Flux ripple at a load of 2.11 N-m.

in the proposed control algorithm by about 67.75% compared with TL-DTC and 33.67%

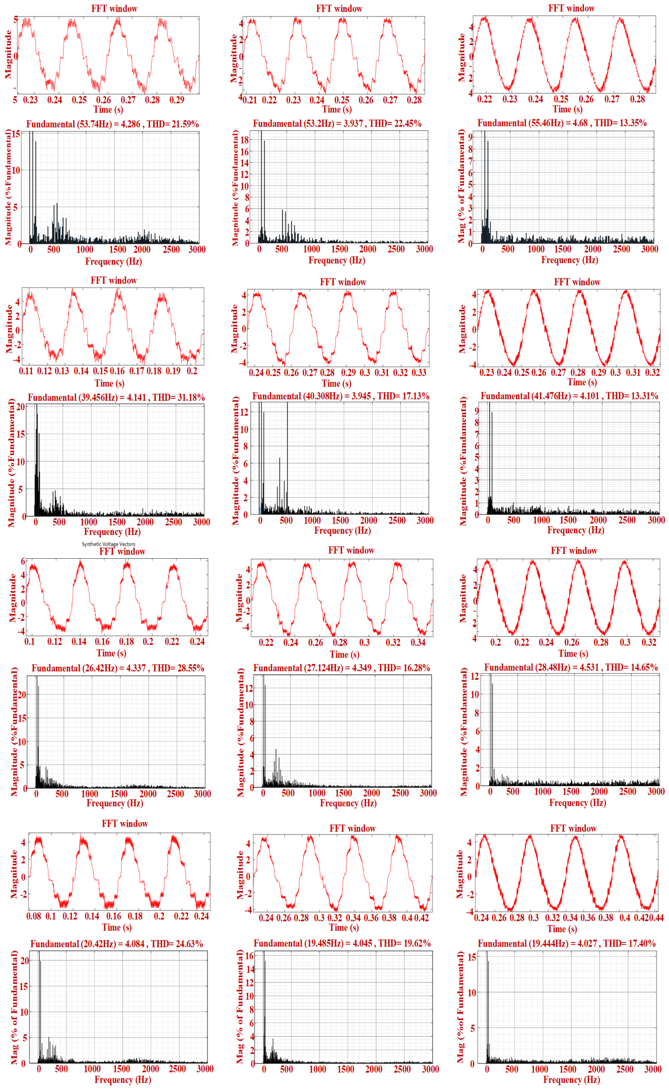

(a) (b) (c)

Fig. 18. FFT spectrum of stator current for a) TL-DTC (Left) b) FL-DTC (middle) c) FCS-MPTC (Right).

2) *Analysis of Stator Current % THD:* The captured results with the help of TEKTRONICS Mixed Domain Oscilloscope 3024 are depicted in Fig. 18, at 1400 r/min, 1000 r/min, 500

TABLE IV
SUMMARY OF TORQUE RIPPLES, FLUX RIPPLES, AND STATOR CURRENT THD

		TL-DTC			FL-DTC			Proposed FCS-MPTC			Reduction of Proposed in (%) Compared with Existing Techniques			
Load	Speed in r/min	Torque Ripple	Flux Ripple	Current %THD	Torque Ripple	Flux Ripple	Current %THD	Torque Ripple	Flux Ripple	Current %THD	Torque Ripple		Flux Ripple	
	1400	0.1833	0.0066	68.30	o.0891	0.0048	35.72	0.0591	0.0035	37.62	67.75	46.97	33.70	27.10
No	1000	0.1612	0.0057	56.59	0.0999	0.0043	23.27	0.0695	0.0041	37.77	56.88	28.07	30.44	4.66
load	500	0.1317	0.0050	50.27	0.0980	0.0043	38.92	0.0677	0.0043	53.55	48.59	30.92	14	0
	200	0.1427	0.0049	57.86	0.1064	0.0044	33.20	0.0804	0.0044	38.85	43.66	24.43	10.20	0
Load	**1400**	**0.1798**	**0.0062**	**21.9**	**0.1244**	**0.0053**	**22.45**	**0.0598**	**0.0033**	**13.35**	**66.74**	**51.93**	**46.77**	**37.74**
0f	**1000**	**0.1598**	**0.0058**	**31.38**	**0.1252**	**0.0046**	**17.13**	**0.06633**	**0.0038**	**13.31**	**60.38**	**49.44**	**34.48**	**17.39**
2.11	**500**	**0.1597**	**0.0054**	**28.55**	**0.1122**	**0.042**	**16.28**	**0.0495**	**0.0034**	**14.65**	**69.00**	**55.88**	**37.03**	**19.04**
N-m	**200**	**0.1505**	**0.0047**	**24.63**	**0.1079**	**0.0041**	**19.62**	**0.0598**	**0.0037**	**17.40**	**60.86**	**45.41**	**21.27**	**9.75**

r/min, and 200 r/min from top to bottom respectively. The harmonic analysis is carried out approximately at a peak current of 4.45 A for the existing and proposed control techniques. The %THD of stator currents is calculated with the help of a .csv file consisting of 10000 samples, the .csv file is obtained from a TEKTRONICS Mixed Domain Oscilloscope. Phase current waveform generated corresponding to data points of .csv file and FFT analysis carried out in MATLAB/Simulink. In TABLE-III it is observed that during no-load the THD of the proposed FCS-MPTC control technique significantly reduced compared with TL-DTC and FL-DTC. Phase current waveforms in the FFT window and %Total Harmonic Distortion (%THD) are shown in Fig. 18 at speeds 1400 r/min, 1000 r/min, 500 r/min, and 200 r/min. Fig. 18(a) TL-DTC [25], displays THD as 21.59%, 31.18%, 28.55%, and 24.63% corresponding speeds to 1400 r/min, 1000 r/min, 500 r/min, and 200 r/min respectively at a load of 2.11 N-m. Fig. 18(b) FL-DTC [26], exhibits the value of THD 22.45%, 17.13%, 16.28%, and 19.62% for the same speeds and load. It can be observed that the suggested FCS-MPTC scheme, shown in Fig. 18(c), shows THD 13.35%, 13.31%, 14.65%, and 17.40%, at speeds of 1400 r/min, 1000 r/min, 500 r/min, and 200 r/min respectively at a load of 2.11 N-m. TABLE-II depicts the THD at no-load and load of 2.11 N-m for TL-DTC, FL-DTC, and FCS-MPTC. Fig. 19 represents the comparison of THD reduction on a bar graph for TL-DTC, FL-DTC, and FCS-MPTC at different speeds of the rotor at a load torque of 2.11 N-m. It is concluded that the proposed FCS-MPTC control technique shows a significant reduction in THD of stator current at both no-load and load of 2.11 N-m, when compared to the present direct torque control techniques TL-DTC, FL-DTC.

3) Reduction of x-y Currents: It is commonly known that x-y subspace (harmonic) currents significantly impact the operation of multi-phase motor drives. To operate the drive at best steady-state performance x-y harmonic currents must be eliminated. Fig. 20 shows an x-y plot for the harmonic currents and fundamental currents at operating speeds of 1400 r/min, 1000 r/min, 500 r/min, and 200 r/min from top to bottom respectively. The smoothness of the outer circle represents the lesser current distortion of fundamental current of drive and the inner circle of the plot having zero radii indicates the elimination of x-y harmonics. In the Fig. 20 right to the reader four vertical plots of the proposed FCS-MPTC (right) have a smoother outer circle and smaller inner circle indicating a minimization of current harmonics than TL-DTC (Left) and FL-DTC (middle). which concludes that the effect of x-y currents is reduced compared with the TL-DTC and FL-DTC.

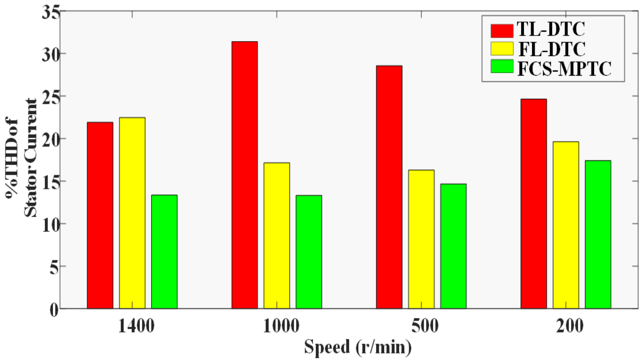

Fig. 19. %THD of stator current at a load of 2.11 N-m.

B. Dynamic Performance Analysis

The dynamic performance of the proposed FCS-MPTC control scheme is tested and compared with the TL-DTC and FL-DTC. The results depicted in Fig. 21. represent the load dynamics of five-phase induction motor drive. when the motor drive runs at 1000 r/min in its steady state, a sudden load of 1.25 N-m is applied in all the methods with help of separately excited DC generator at reduced excitation and lamp loads of different wattage. It is noticed in Fig. 21. TL-DTC (left) and FL-DTC (middle) methods the peak load torque (2 N-m), and

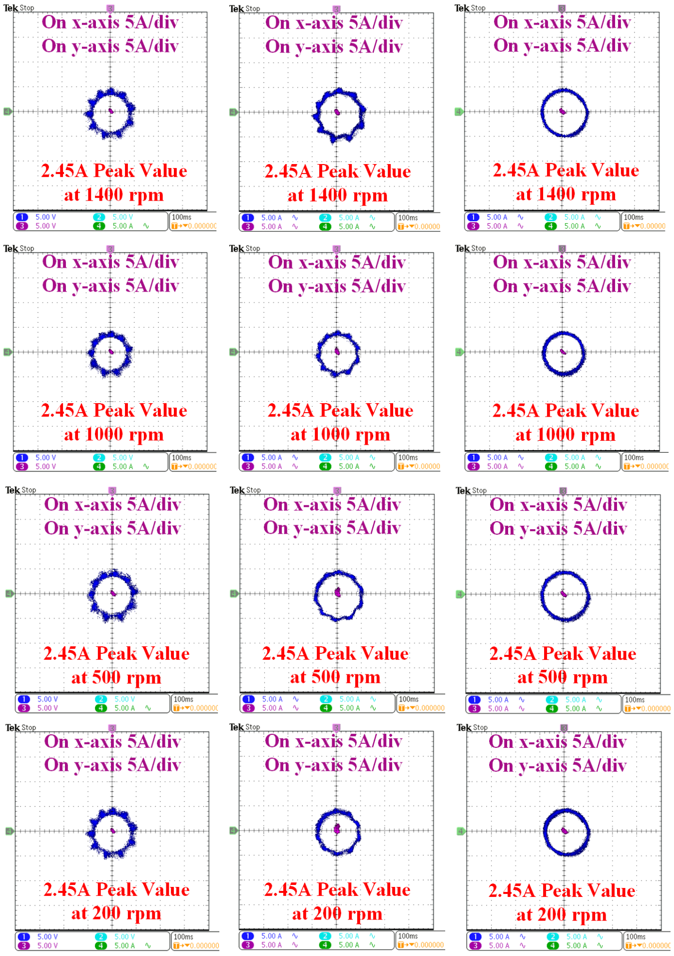

(a) (b) (c)

Fig. 20. FFT spectrum of stator current for a) TL-DTC (Left) b) FL-DTC (middle) c) FCS-MPTC (Right).

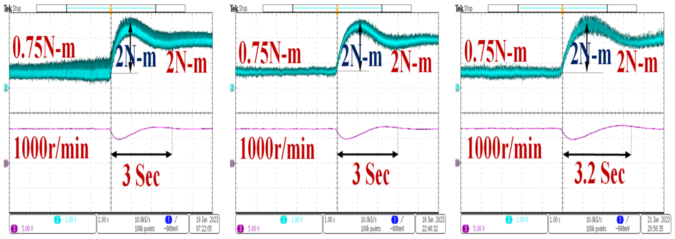

(a) (b) (c)

Fig. 21. Load dynamics at 1000 r/min, 2 N-m for a) TL-DTC(Left) b) FL-DTC(Middle) c) FCS-MPTC(Right).

settling times (3 sec) are observed as same but in FCS-MPTC (right) is shows 0.2 sec higher in settling time which will not significantly affect dynamic behavior of the drive.

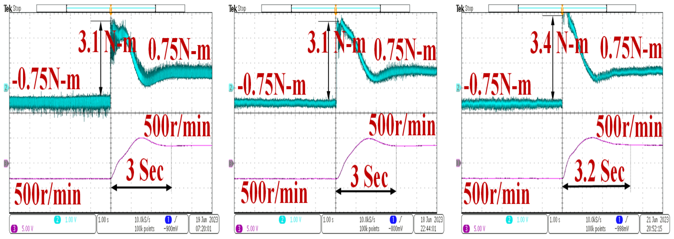

(a) (b) (c)

Fig. 22. Speed reversal from -500 r/min to 500 r/min for a) TL-DTC(Left) b) FL-DTC(Middle) c) FCS-MPTC(Right).

V. CONCLUSION

The proposed dual five-leg inverter-fed Five-Phase Open-End Winding (FPOEW) Induction Motor topology significantly improves steady-state performance by reducing torque ripple, flux ripple, and stator current Total Harmonic Distortion (THD) without using a higher number of levels and sectors. Using active medium and large voltage vectors as virtual vectors enhances the DC bus utilization and eliminates Common Mode Voltage (CMV) across motor windings. The x-y harmonic plane components were further reduced with a cost function-based approach rather than the volt-sec balance method. The Finite Control Set Model Predictive Torque Control (FCS-MPTC) technique, with a shared DC link between inverters, further ensures zero common mode current, removing the need for an isolation transformer and suppressing high harmonic currents. Compared to traditional Three-Level and Five-Level Direct Torque Control (TL-DTC and FL-DTC) methods, FCS-MPTC demonstrates superior performance. The research is particularly relevant for high-performance applications like Electric Hybrid Vehicles (EHV), submarines, and aircraft.

REFERENCES

[1] G.K Singh, Multi-phase induction machine drive research—a survey, Electric Power Systems Research, Volume 61, Issue 2,2002, Pages 139-147, ISSN 0378-7796, https://doi.org/10.1016/S0378-7796(02)00007-X

[2] L. Parsa, "On advantages of multi-phase machines," 31st Annual Conference of IEEE Industrial Electronics Society, 2005. IECON 2005., Raleigh, NC, USA, 2005, pp. 6 pp.-, doi: 10.1109/IECON.2005.1569139.

[3] M. Y. Metwly, A. S. Abdel-Khalik, M. S. Hamad, S. Ahmed, and N. A. Elmalhy, "Multiphase Stator Winding: New Perspectives, Advanced Topologies, and Futuristic Applications," in IEEE Access, vol. 10, pp. 103241-103263, 2022, doi: 10.1109/ACCESS.2022.3209372.

[4] A. Li, D. Jiang, Z. Liu, X. Sun and W. Kong, "Unified Analysis of Winding Connection Sequence in Series-End Winding Topology," in IEEE Transactions on Industry Applications, vol. 57, no. 1, pp. 516-527, Jan.-Feb. 2021, doi: 10.1109/TIA.2020.3032936. doi:10.1109/TPEL.2014.2304561

[5] V. Kumar and S. Kumar, "A Novel Multilevel Inverter Fed Open-End Winding Coupled-Induction Motor Drive for Sugar Industry," in IEEE Transactions on Energy Conversion, vol. 38, no. 4, pp. 2706-2716, Dec. 2023, doi: 10.1109/TEC.2023.3294301.

[6] K. Rahman et al., "Field-Oriented Control of Five-Phase Induction Motor Fed from Space Vector Modulated Matrix Converter," in IEEE Access, vol. 10, pp. 17996-18007, 2022, doi: 10.1109/ACCESS.2022.3142014.

[7] V. s. r. Chagam redd and S. Devabhaktuni, "Reduction of Stator Flux Ripple and Current Harmonic Distortion using Constant Switching Flux Controller-based DTC of Five-Phase Induction Motor," in IEEE Latin America Transactions, vol. 21, no. 8, pp. 915-924, Aug. 2023, doi: 10.1109/TLA.2023.10246341.

[8] K. M. R. Eswar, K. V. P. Kumar and T. V. Kumar, "A Simplified Predictive Torque Control Scheme for Open-End Winding Induction Motor Drive," in IEEE Journal of Emerging and Selected Topics in Power Electronics, vol. 7, no. 2, pp. 1162-1172, June 2019, doi: 10.1109/JESTPE.2018.2832240.
[9] N. Rayavarapu, S. Devabhaktuni and C. V. Subba Reddy, "Weighting Factor Less Model Predictive Flux Control of Five-Phase Induction Motor with Maximum Torque per Ampere," 2023 11th National Power Electronics Conference (NPEC), Guwahati, India, 2023, pp. 1-6, doi: 10.1109/NPEC57805.2023.10384900.
[10] A. Bhowate, M. V. Aware and S. Sharma, "Predictive Torque Control of Five-Phase Induction Motor Drive Using Successive Cost Functions for CMV Elimination," in IEEE Transactions on Power Electronics, vol. 36, no. 12, pp. 14133-14141, Dec. 2021, doi: 10.1109/TPEL.2021.3089741.
[11] V. S. Reddy Chagam and S. Devabhaktuni, "Enhanced Low-Speed Characteristics with Constant Switching Torque-Controller-Based DTC Technique of Five-Phase Induction Motor Drive with FOPI Control," in IEEE Transactions on Industrial Electronics, vol. 70, no. 11, pp. 10789-10799, Nov. 2023, doi: 10.1109/TIE.2022.3227275.
[12] Y. Luo and C. Liu, "A Simplified Model Predictive Control for a Dual Three-Phase PMSM with Reduced Harmonic Currents," in IEEE Transactions on Industrial Electronics, vol. 65, no. 11, pp. 9079-9089, Nov. 2018, doi: 10.1109/TIE.2018.2814013.
[13] A. Ray, S. Belkhode, R. Karampuri and S. Jain, "Optimized PWM Techniques with 3rd Harmonic Injection for Five Phase Concentrated Winding Induction Motor with Open-End Stator," 2018 IEEE International Conference on Power Electronics, Drives and Energy Systems (PEDES), Chennai, India, 2018, pp. 1-6, doi: 10.1109/PEDES.2018.8707549.
[14] Y. N. Tatte and M. V. Aware, "Torque Ripple and Harmonic Current Reduction in a Three-Level Inverter-Fed Direct-Torque-Controlled Five-Phase Induction Motor," in IEEE Transactions on Industrial Electronics, vol. 64, no. 7, pp. 5265-5275, July 2017, doi: 10.1109/TIE.2017.2677346.
[15] U. R. Muduli, R. K. Behera, K. Al Hosani and M. S. E. Moursi, "Direct Torque Control with Constant Switching Frequency for Three-to-Five Phase Direct Matrix Converter Fed Five-Phase Induction Motor Drive," in IEEE Transactions on Power Electronics, vol. 37, no. 9, pp. 11019-11033, Sept. 2022, doi: 10.1109/TPEL.2022.3167477.
[16] S. Payami and R. K. Behera, "An Improved DTC Technique for Low-Speed Operation of a Five-Phase Induction Motor," in IEEE Transactions on Industrial Electronics, vol. 64, no. 5, pp. 3513-3523, May 2017, doi: 10.1109/TIE.2017.2652397.
[17] Y. N. Tatte and M. V. Aware, "Direct Torque Control of Five-Phase Induction Motor with Common-Mode Voltage and Current Harmonics Reduction," in IEEE Transactions on Power Electronics, vol. 32, no. 11, pp. 8644-8654, Nov. 2017, doi: 10.1109/TPEL.2016.2644988.
[18] J. A. Riveros, F. Barrero, E. Levi, M. J. Durán, S. Toral and M. Jones, "Variable-Speed Five-Phase Induction Motor Drive Based on Predictive Torque Control," in IEEE Transactions on Industrial Electronics, vol. 60, no. 8, pp. 2957-2968, Aug. 2013, doi: 10.1109/TIE.2012.2198034.
[19] MA. Bhowate, M. V. Aware and S. Sharma, "Predictive Torque Control Algorithm for a Five-Phase Induction Motor Drive for Reduced Torque Ripple with Switching Frequency Control," in IEEE Transactions on Power Electronics, vol. 35, no. 7, pp. 7282-7294, July 2020, doi: 10.1109/TPEL.2019.2954991.
[20] A. Bhowate, M. V. Aware and S. Sharma, "Speed Sensor-Less Predictive Torque Control for Five-Phase Induction Motor Drive Using Synthetic Voltage Vectors," in IEEE Journal of Emerging and Selected Topics in Power Electronics, vol. 9, no. 3, pp. 2698-2709, June 2021, doi: 10.1109/JESTPE.2020.3016335.
[21] F. Khoucha, S. M. Lagoun, K. Marouani, A. Kheloui and M. E. H. Benbouzid, "Hybrid Cascaded H-Bridge Multilevel-Inverter Induction-Motor-Drive Direct Torque Control for Automotive Applications," in IEEE Transactions on Industrial Electronics, vol. 57, no. 3, pp. 892-899, March 2010, doi: 10.1109/TIE.2009.2037105.
[22] M. F. Escalante, J.C. Vannier and A. Arzande, "Flying capacitor multilevel inverters and DTC motor drive applications," in IEEE Transactions on Industrial Electronics, vol. 49, no. 4, pp. 809-815, Aug. 2002, doi: 10.1109/TIE.2002.801231.
[23] I. Harbi et al., "Model-Predictive Control of Multilevel Inverters: Challenges, Recent Advances, and Trends," in IEEE Transactions on Power Electronics, vol. 38, no. 9, pp. 10845-10868, Sept. 2023, doi: 10.1109/TPEL.2023.3288499.
[24] P. C. Mavila and P. P. Rajeevan, "A New Direct Torque Control Scheme for Five Phase Open-end Winding Induction Motor Drives with Reduced DC Voltage Requirement," 2020 IEEE International Conference on Power Electronics, Smart Grid and Renewable Energy (PESGRE2020), Cochin, India, 2020, pp. 1-6, doi: 10.1109/PESGRE45664.2020.9070665.
[25] Reddy, C.V.S., Devabhaktuni, S. (2022). Low-Speed Performance Improvement of Dual VSI Fed Direct Torque Controlled Five Phase Open-End Winding Induction Motor. In: Kumar, S., Singh, B., Singh, A.K. (eds) Recent Advances in Power Electronics and Drives. Lecture Notes in Electrical Engineering, vol 852. Springer, Singapore. https://doi.org/10.1007/978-981-16-9239-0_20.
[26] P. C. Mavila and P. P. Rajeevan, "A Five-Level Torque Controller Based DTC Scheme for Open-End Winding Five-Phase IM Drives with Single DC Source and Auxiliary Plane Harmonic Elimination," in IEEE Transactions on Industry Applications, vol. 58, no. 2, pp. 2063-2074, March-April 2022, doi: 10.1109/TIA.2022.3140361.
[27] P. C. Mavila and R. P. P., "A Virtual Vector Based DTC Scheme with Enhanced Resolution for Dual Inverter Fed Five-Phase IM Drives," in IEEE Journal of Emerging and Selected Topics in Industrial Electronics, vol. 4, no. 2, pp. 669-677, April 2023, doi: 10.1109/JESTIE.2022.3215761.
[28] V. S. Reddy Chagam and S. Devabhaktuni, "An Isolation Transformerless Single DC Source fed Dual 5-leg Inverter Controlled 5-Phase Induction Motor with Modified Direct Torque Control," in IEEE Latin America Transactions, vol. 22, no. 3, pp. 229-239, March 2024, doi: 10.1109/TLA.2024.10431418.
[29] P. Cortes et al., "Guidelines for weighting factors design in Model Predictive Control of power converters and drives," 2009 IEEE International Conference on Industrial Technology, Churchill, VIC, Australia, 2009, pp. 1-7, doi: 10.1109/ICIT.2009.4939742.

Naresh Rayavarapu was born in Kaza near Machilipatnam India in 1987. He received his Master's Degree (2016) in power electronics and Electrical Drives from JNTU Hyderabad. Currently working on, a Ph.D. degree from the Electrical Engineering Department, National Institute of Technology, Warangal, India. His current work interests are Power Electronics and Drives.

Swati Devabhaktuni (Member, IEEE) received a Ph.D. degree in electrical engineering from the JNT University, Hyderabad in 2014. Currently, she is working as an Assistant professor at the National Institute of Technology, Warangal. Her research interests are power electronics, AC motor drives, and control systems.

Venkata Subba Reddy C. was born in Kadapa, India in 1991. He received his Master's Degree (2015) in Power Electronics Drives from RGMCET Nandyal. Currently, he is working towards a Ph.D. degree from the Electrical Engineering Department, National Institute of Technology, Warangal, India. His current research work interests are speed control of multi-phase drives.